Neutral-atom-scattering-based mapping of atomically thin layers

Geetika Bhardwaj, Krishna Rani Sahoo, Rahul Sharma, Parswa Nath, and Pranav R. Shirhatti[*]

Tata Institute of Fundamental Research Hyderabad, 36/P Gopanpally, Hyderabad 500046, Telangana, India

Imaging surfaces using low-energy neutral atom scattering is a relatively recent development in the field of microscopy. In this paper, we demonstrate that this technique is sensitive enough to distinguish films as thin as a single monolayer from the underlying substrate. Using collimated beams of He and Kr atoms as an incident probe on MoS_2 films grown on SiO_2/Si substrates, we observe systematic changes in the scattered atom flux which allows us to map the thin MoS_2 films. Measurements carried out by varying incidence energy using both He and Kr provides insights into the details of atom-surface collision dynamics and its role in contrast generation.

I. INTRODUCTION

Developments in microscopy and imaging techniques have made a profound impact on our understanding of a wide range of physical phenomena. The variety of techniques developed over the years is impressive, such as the light microscope [1], sub-Å level resolution electron microscopes [2,3], and surface probe techniques such as atomic force and scanning tunneling microscopes [4–7] to name a few. A relatively recent addition to this gamut of microscopy techniques is neutral atom microscopy, also known as scanning Helium microscopy, when He atoms are used as an incident probe [8–11]. Its foundations lie in the scattering of low-energy neutral atoms from surfaces, an area pioneered by Estermann and Stern many decades ago [12].

Unique features of NAM as an imaging technique are that it is nondestructive and universally applicable. The typical kinetic energy of incident neutral atoms used as a probe range from ten to a few hundred meV. Being at least an order of magnitude smaller than chemical bond energies ($\sim$ few eV), it is particularly well suited for imaging delicate surface structures otherwise susceptible to beam-induced damage.

Given that the de Broglie wavelength of atoms at kinetic energies in the above-mentioned range is of the order of Å, in principle, a very high resolution imaging is possible using this approach. In practice though, the achievable resolution is primarily constrained by the limited ability to manipulate the motion of incident neutral atoms. Nonetheless, improvements in detector design [13] and experimental schemes to manipulate the incident atoms [14–16] hold enormous promise in achieving spatial resolution, well into the sub-100 nm range and beyond.

Another fundamental aspect of NAM that needs to be looked into further to realize its full potential is to understand the contrast generation mechanisms leading to image formation. Contrast (C) is a measure of the ability to distinguish different features observed in an image and is defined as the normalized difference in signals I_1 and I_2 observed from two different surface features [8] as shown below:

$$C = \left| \frac{I_1 - I_2}{I_1 + I_2} \right|. \tag{1}$$

One of the most commonly observed features in NAM images is that of topographical contrast. This results from a change in the detected signal caused by changes in diffuse scattering due to different geometric features on the surface [8]. Contrast arising from the changes in scattering distributions resulting from inelastic collisions has also been identified [17]. More recently, contrast resulting via atomic diffraction by the crystalline nature of target sample has also been demonstrated [18]. This opens up the possibility of seeing features beyond the capability of conventional imaging methods. It is well known that atom scattering from surfaces is sensitive to local surface structure and disorder at an atomic length scale [19] and, in principle, can be utilized for contrast generation. However, it is generally expected that to observe these effects, precisely prepared clean surfaces under ultrahigh vacuum conditions are needed.

In this paper, we study atom-scattering-based imaging of thin MoS_2 films grown on SiO_2/Si substrates. We take advantage of the fact that such two-dimensional (2D) materials are relatively chemically inert and need less stringent working conditions [20]. Our results demonstrate that MoS_2 films, as thin as a single monolayer, can be distinguished from the substrate and mapped by means of measuring changes in the scattered atom flux. Further insights into collision dynamics and contrast generation are obtained from incidence energy (E_{inc}) dependent measurements, using both He (light) and Kr (heavy) atoms as probes.

II. METHODS

A. Instrument setup

Our NAM apparatus produces a collimated atomic beam using a series of pinholes, similar to the designs reported previously [9,10]. This beam scatters from the sample surface mounted on a movable platform comprising two piezo-driven stages (ECSx3030/NUM(+), Attocube). Scattered atoms are detected as a function of sample position by a mass spectrometer (RGA200, Stanford Research Systems) arranged in a flux

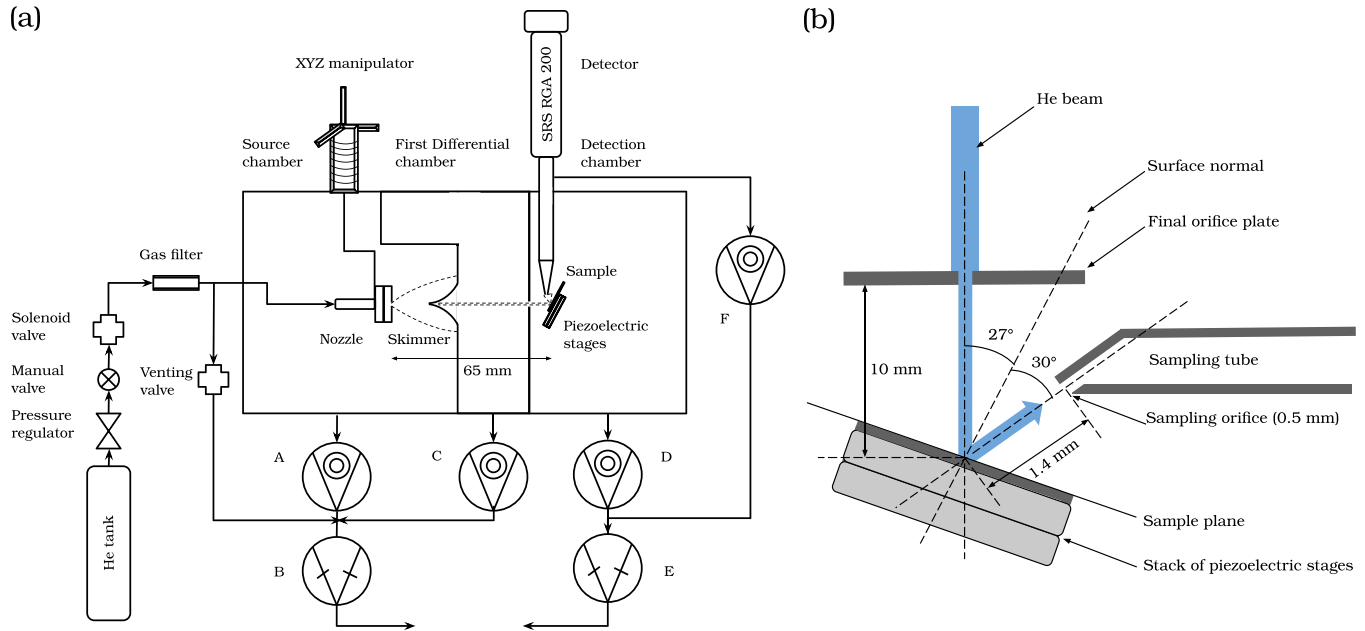*Corresponding author: pranavrs@tifrh.res.in

(a)

(b)

FIG. 1. (a) Block diagram of our experimental setup for NAM. He gas at stagnation pressure (typically 6 bar) is allowed to expand supersonically using a $20\,\mu$m nozzle in the source chamber. Gas is passed through a $0.5\,\mu$m filter to avoid any clogging. Nozzle position can be optimized using an XYZ manipulator. Atomic beam is collimated by a $200\,\mu$m opening skimmer and a $20\,\mu$m aperture before reaching the sample. Scattered atoms from the target are collected by a sampling aperture connected to a mass spectrometer (flux detection). (b) A detailed view of the scattering geometry used in our experiments. Incident He beam and sampling aperture are at an angle of $27°$ and $30°$ with respect to the surface normal, respectively. Collection angle of the sampling orifice spans a range of approximately $20°$. Sample holder is attached to a pair of piezo-driven stages which enables us to perform a raster scan to obtain a map of partial pressure versus sample position, leading to NAM images

detection mode. Figure 1(a) shows a block diagram of the experimental setup comprising all essential elements from the atomic beam source to the detector. These stages are arranged sequentially as source, differential, scattering, and stagnation detector. These are pumped by turbo molecular pumps (denoted by A, C, D, and F) with nominal pumping speeds of $1200\,$l/s (HiPace 1200, Pfeiffer Vacuum), $300\,$l/s (Twistorr 305, Leybold), $300\,$l/s (HiPace 300, Pfeiffer Vacuum) and $80\,$l/s (HiPace 80, Pfeiffer Vacuum), respectively. A $35\,$m^3/hr rotary vane pump (Duo 35, Pfeiffer Vacuum) was used to back the source and differential chambers, respectively. Scattering and detection stages were backed by an $11\,$m^3/hr rotary vane pump (Duo 11, Pfeiffer Vacuum).

Atomic beams of He and Kr were produced by a continuous nozzle as the source, built by sandwiching a circular metal film (Lenox Laser Inc.) with an orifice diameter of $20\,\mu$m (thickness $30\,\mu$m) between two metal plates. The beam is extracted into a differentially pumped chamber using a skimmer (Beam Dynamics, Model 2) with orifice diameter of $200\,\mu$m. Another metal film having a $20\,\mu$m diameter orifice was used to collimate the beam before entering into the scattering chamber. The source to sample distance was approximately 65 mm. Incident beam cross-sectional diameters were measured using a knife-edge scan on the sample plane, approximately 10 mm away from the final aperture. Cross-sectional diameters (full width at half maximum, FWHM) ranged from 27 to 33 μm (Table I), corresponding to a narrow angular divergence of ~ 1 mrad (see Appendix A).

Typical steady-state pressures in the source, differential stages were 2×10^{-8} mbar, 1×10^{-8} mbar with beam off and

1×10^{-4} mbar, and 1×10^{-6} mbar with beam on, respectively (pure He, backing pressure 6 bar). Pressure increase in the scattering chamber with beam on (measured with an ionization gauge) remained below our detection limit with the pressure being 1×10^{-7} mbar. The background He partial pressure (beam off) detected was typically around 1.25×10^{-12} mbar. With the beam on, the detected He partial pressure was 1.55×10^{-12} mbar (target sample removed). Considering this change, we estimate that a total of 2.2×10^9 atoms/s are incident on the target surface corresponding to a flux of 7×10^{14} atoms/(s str) (Appendix B).

For varying $E_{\rm inc}$, seeded beams of helium and krypton with different compositions were employed. These were prepared by mixing the constituent gases in the appropriate ratio of partial pressures in a stainless steel reservoir and care was taken to allow the gases to mix for at least 6–8 hours prior to any measurement. $E_{\rm inc}$ of He and Kr ranged from 9 to 65 meV and 124 to 453 meV, respectively (Table I). The terminal velocity (v_∞) of the gas mixture was estimated using the following relation [21]:

$$v_\infty = \sqrt{\frac{2R}{\langle m \rangle}\left(\frac{\gamma}{\gamma - 1}\right)T_0},\qquad (2)$$

where $\langle m \rangle$ is atomic mass of the gas (weighted average mass in case of mixtures), R is the universal gas constant, γ is the ratio of specific heats, and T_0 is the stagnation temperature. $E_{\rm inc}$ of He or Kr in a given gas mixture was calculated as $\frac{1}{2}\, m_i v_\infty^2$, where m_i corresponds to the mass of the ith component (He or Kr).

TABLE I. Incident kinetic energy (E_{inc}) of He and Kr in meV and their cross-sectional diameters in μm [full width half maximum, (FWHM)] on the sample plane for different atomic beams used in this paper. E_{inc} values were calculated using Eq. (2) and beam diameters were estimated from knife-edge scan measurements (Appendix A). Uncertainties correspond to standard error obtained from fitting. The He beam at $E_{inc} = 6$ meV was not used in the present experiments due to its low incident flux.

Composition	E_{inc}(He)	E_{inc}(Kr)	Cross section diameter, FWHM, (He, Kr)
100% He	65		26.9 ± 0.5, –
10% Kr + 90% He	22	453	30.8 ± 1.2, 28.9 ± 0.7
20% Kr + 80% He	13	272	29.5 ± 2.2, 30.4 ± 0.8
30% Kr + 70% He	9	194	28.8 ± 2.6, 29.9 ± 0.8
50% Kr + 50% He	6	124	–, 33.4 ± 1.2

Arrangement of the incident beam, sample positioning, and detection is depicted in Fig. 1(b). The sampling aperture is placed approximately along the specular direction with an incident and detection angle of $(27 \pm 1.5)°$ and $(30 \pm 1.5)°$ with respect to the surface normal, respectively. The sampling aperture collects the scattered flux over a relatively large span of 20°, which is comprised of specular reflected signal (zeroth-order diffraction) and diffuse elastic and inelastic scattering components (see Results and Discussion for more details). A LabView-based program was used to acquire real-time data from the mass spectrometer and to control the positioning of stages.

B. Sample preparation and characterization

Chemical vapor deposition (CVD) method [22] was used to grow thin films of molybdenum disulfide (MoS_2) on 300-nm-thick silicon dioxide (SiO_2) grown on a Si(100) substrate (MicroChem Pvt. Ltd). Four-mg ultrapure molybdenum trioxide (99.97%, Sigma-Aldrich) and 300 mg sulfur powder (99.99% pure, Sigma-Aldrich) were used as precursors (see Appendix C for details). Raman spectroscopic characterization of the samples was done using Renishaw inVia confocal Raman microscope with objectives of 5x and 50x (long focal length). The spectrometer has a spectral resolution of $0.5\,cm^{-1}$ with a focal spot diameter of $2\,\mu$m. An excitation wavelength of 532 nm with 2 mW power was used. Acquisition time was set to 20–50 s for a desired signal-to-noise ratio and measurement speed.

MoS_2 thin-film samples used in this work were transferred into the vacuum chamber within 48 hours of preparation. Scattered He flux and contrast obtained from thin MoS_2 films with respect to the SiO_2/Si substrate were observed to remain largely unchanged over a span of six days. For a given sample, care was taken to complete one set of measurements within this time span (see Appendix D). For durations longer than 12 to 14 days, a systematic decrease in contrast obtained using He was observed. This indicates gradual changes in the sample, possibly caused by hydrocarbon, water adsorption, and/or chemical degradation.

III. RESULTS AND DISCUSSIONS

A. Characterization of thin films using optical microscopy and Raman spectroscopy

Films of MoS_2 on SiO_2/Si substrates, prepared by the CVD method, were characterized using optical microscopy and Raman spectroscopy. An optical image of a small portion of the sample, obtained using white light illumination, is shown in Fig. 2(a). Two distinct features of MoS_2 films are visible, namely, blue and light-blue colored regions on the purple colored substrate. Raman spectra measured in the regions of interest [center of black circles in Fig. 2(a), 2 μm diameter illuminated spot] are shown in Fig. 2(b). Spectra obtained for regions 2 and 3 show two additional peaks within (380 to 410) cm^{-1} compared to that for region 1, where a single peak at 521 cm^{-1} corresponding to SiO_2/Si [23] is seen, confirming the presence of MoS_2 films. The two peaks within (380 to 410) cm^{-1} correspond to in-plane and out-of-plane vibrational modes of MoS_2 with E_{2g}^1 and A_{1g} symmetry [24], respectively.

With an increasing number of layers, E_{2g}^1 and A_{1g} modes are known to exhibit a red and blue shift, resulting in a characteristic peak separation as a function of layer thickness [25,26]. For samples used in our experiments, peak separation observed in the case of thin films was (19 to 20) cm^{-1}, whereas for thick bulklike films, it was (25 to 26) cm^{-1} (see Appendix E). Comparing with previously reported frequency shifts as a function of layer thickness, we conclude that blue colored regions (region 2) correspond to one to two monolayer thickness and light-blue colored regions (region 3) correspond to thicker bulklike layers (greater than six monolayers).

B. NAM measurements and contrast generation mechanisms

Optical microscopy images of three independently prepared samples along with Raman spectra are shown in Figs. 3(a)–3(c) and Figs. 3(g)–3(i), respectively. As seen previously, in all the samples, bare substrate, thin films, and thick films of MoS_2 can be identified using Raman spectroscopy. NAM images of the same, obtained by measuring scattered He flux, are depicted in Figs. 3(d)–3(f). It can be seen quite clearly that scattered He flux from regions covered with MoS_2, irrespective of layer thickness, is consistently higher by 15–30% than that from the bare substrate. A clear one-to-one correspondence among the optical and NAM images can be seen. The key point here is that regions with MoS_2 films, as thin as a single monolayer, can be clearly distinguished from the substrate by means of change in scattered He flux captured by our detector.

An important question arising here is regarding the nature of contrast-generating mechanism. Before delving into an interpretation of our experimental observations, we briefly discuss some basic aspects of the atom–surface-scattering
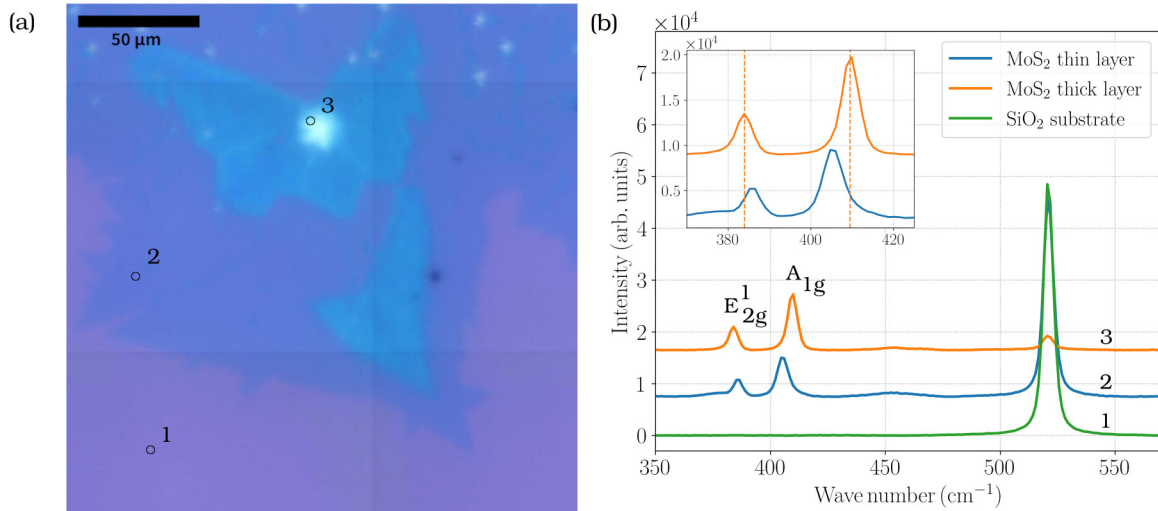
FIG. 2. (a) Optical microscopy image of MoS_2 films grown on SiO_2/Si substrate (using white light illumination). Three distinct regions with colors purple (region 1), blue (region 2), and light-blue (region 3) correspond to SiO_2/Si substrate, thin and thick MoS_2 films, respectively. (b) Raman spectra (measured using 2 μm focal spot diameter) observed at three different regions, measured at positions marked by centers of black circles 1, 2, and 3 shown in (a). The corresponding spectra (marked as 1, 2, and 3) have been offset along the vertical axis for clarity. In the inset, shifts in the vibrational modes for thin (lower curve) and thick (upper curve) MoS_2 films are clearly visible. Vertical dotted lines correspond to the peak positions of thick (bulklike) MoS_2 films. We assign thin layers to be comprised of one to two monolayers (see text for details).

process, relevant for the question posed above. An excellent overview of these points is provided in Refs. [19,27] and references within.

Scattering of atoms from surfaces can be broadly classified into being elastic and inelastic. Elastic scattering is a particularly important channel for lighter particles such as He atoms (and H_2 and D_2). On well-defined pristine surfaces with large flat domains and low defect density, such as polished and/or cleaved single crystals, He atoms largely undergo elastic scattering. This results in characteristic diffraction patterns, with the zeroth order peak in the specular direction (mirror reflection) being as intense as up to 50% relative to the incident beam [28–30]. On the other hand, for heavier atoms such as Ar, Kr, Xe, etc., it is well established that elastic scattering is a relatively minor channel (∼1%) [29,31–33]. It can only be distinguished from the relatively larger inelastic scattering fraction by working at low incidence energies and surface temperatures which suppress the inelastic components and thermal broadening, respectively.

On surfaces with defects such as steps, dislocations, grain boundaries, and point defects caused by missing atoms and the presence of adsorbates, incident He atoms undergo diffuse elastic scattering. Cross sections for diffuse elastic scattering of He atoms due to adsorbates are much larger than their geometric counterparts, with values in the range of a few hundred $Å^2$. Further, these cross sections are known to increase with decreasing E_{inc} [19,34], leading to a reduction in specular scattered flux at lower E_{inc}.

Inelastic scattering mainly arises from the energy exchange of atoms with vibrations of surface atoms or adsorbates. For lighter atoms such as He, this component becomes increasingly important at lower E_{inc}, comparable to the lattice vibration energies. For heavier particles such as Kr atoms, traveling with relatively higher energies as in our experiments,

it usually manifests as an energy loss and a relatively broader angular distribution, peaked away slightly from the true specular direction, depending on the momentum exchanged in the collision process [29].

Finally, we would like to point out that in scattering from macroscopically rough surfaces where multibounce collisions dominate, elastically scattered flux distributions will also be diffuse. For heavier atoms, a large overall energy loss is expected due to multiple inelastic collisions and can possibly lead to trapping. Several of the above points need to be considered to understand the contrast generation and its E_{inc} dependence observed in our experiments, both with light He and heavier Kr atoms.

In our experimental setup, the collection angle spans approximately 20° about the specular reflection direction. Assuming that diffuse scattering (elastic or inelastic) follows a cosine distribution, we estimate that our detector collects about 2% of the total diffuse scattered flux. On the other hand, the true specular scattered flux having a much narrow angular distribution ($\ll$ 1°) will be completely captured by our detector. Previously reported He scattering studies from clean single-crystal MoS_2 surfaces under ultrahigh vacuum conditions [35] show that specular reflected intensity is of the order of 2% at 300 K. Since samples in our experiments are far from being under pristine conditions, this represents an upper limit to the true specular scattered flux seen by our detector. Consequently, it is possible that the small fraction of diffuse scattered flux and true specular scattered flux reaching our detector are of comparable magnitude. This presents several interesting possibilities for contrast generation and its E_{inc} dependence which are discussed below.

At the outset, it is useful to estimate the expected contrast for MoS_2 and SiO_2/Si surfaces using He as a probe, assuming that variations in specular intensity is the sole contributing
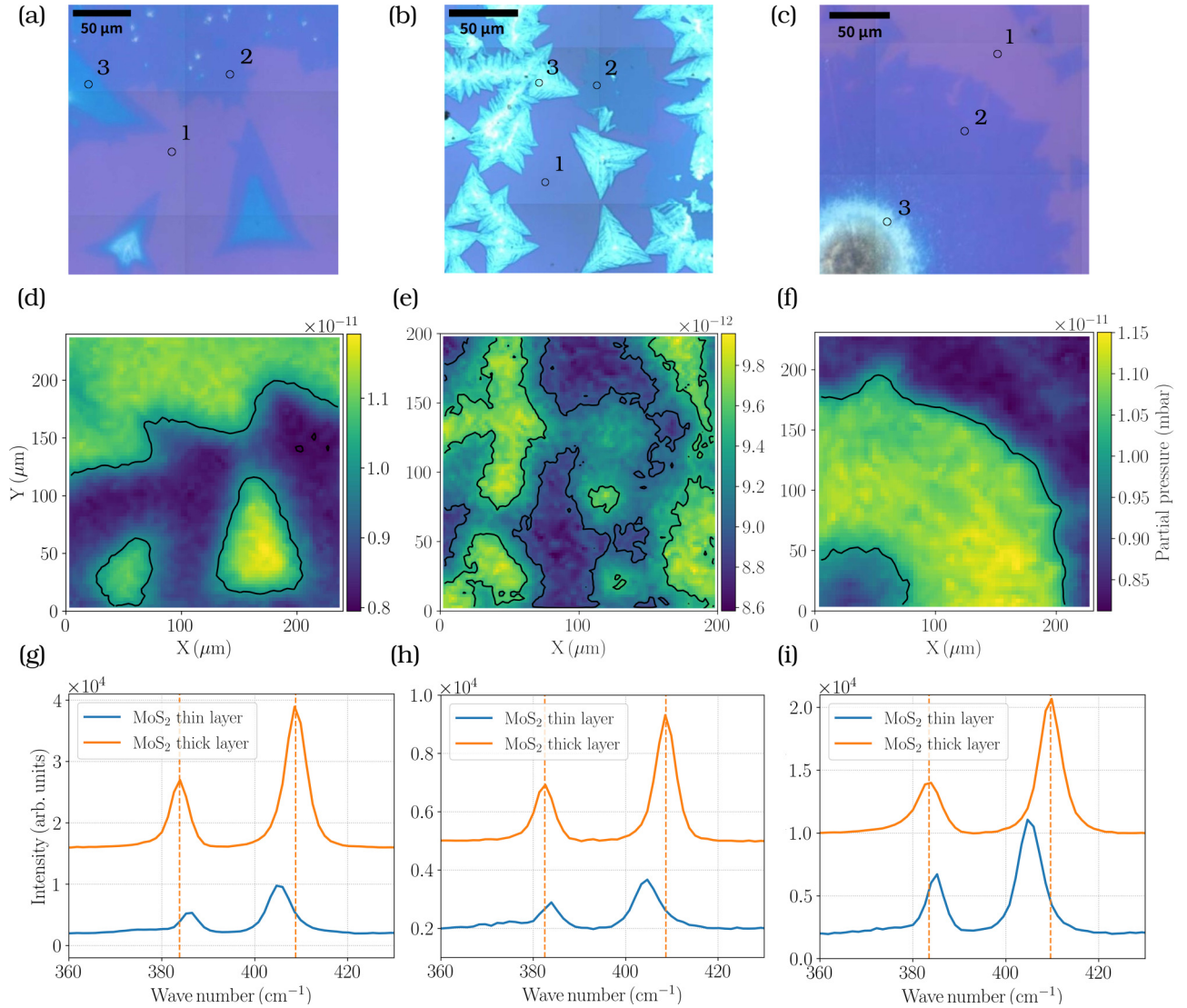
FIG. 3. (a)–(c) Optical microscopy images obtained using three independently prepared samples. (d)–(f) Corresponding NAM images using He, measured with step sizes of $6\,\mu$m, $4\,\mu$m, and $7\,\mu$m, respectively. The data is linearly interpolated and, depending on the features of interest, two or three isopartial pressure contour lines are plotted to illustrate the correlated regions. (g)–(i) Raman spectra measured at the points represented by the centers of black circles (regions 2 and 3) shown in (a)–(c). The upper and lower curves correspond to thick and thin MoS_2 layers, respectively. Observed peak separations show the presence of a single monolayer (thin) and bulklike MoS_2 (thick) films. A clear one-to-one correspondence among optical and NAM images can be seen. Regions comprising MoS_2 films, as thin as a single monolayer, can be clearly distinguished from the substrate in NAM images.

factor. One should note that this picture is strictly valid only for the case where surfaces are in pristine condition. Since our samples are likely to have defects and adsorbates, this merely represents a limiting scenario. Specular scattered intensity of He can be estimated using the Debye Waller factor [19,28]. Resulting contrast from two surfaces a and b with atomic masses M_a and M_b, having Debye temperatures of Θ_a and Θ_b, is governed by the following relation [8]:

$$C = \tanh\left[\frac{\alpha}{2}\left(\frac{1}{M_a\Theta_a^2} - \frac{1}{M_b\Theta_b^2}\right)\right], \qquad (3)$$

where

$$\alpha = \frac{24m(E_{inc}\cos^2\theta_{inc} + D)T_s}{k_B}. \qquad (4)$$

Here, m = mass of incident atom (He), E_{inc} = incident energy, θ_{inc} = incident angle, D = depth of the attractive potential (assumed to be same for both surfaces a and b), T_s = surface temperature, k_B = Boltzmann constant.

Unlike surfaces composed of a single kind of atom, in the present case it is not clear *a priori* what the values of M_a and M_b would be. Nevertheless, a qualitative estimate can be made as discussed below. For MoS_2, based on the attenuation of specular He intensity versus surface temperature [35], we obtain an effective surface mass in the range of 210–240 amu. Given that the He signal for SiO_2/Si surface is comparatively lower by 10–30%, the range of surface mass of SiO_2/Si which satisfies this constraint is around 60 amu. This leads to an estimated contrast in the range of 5–15%, which decreases
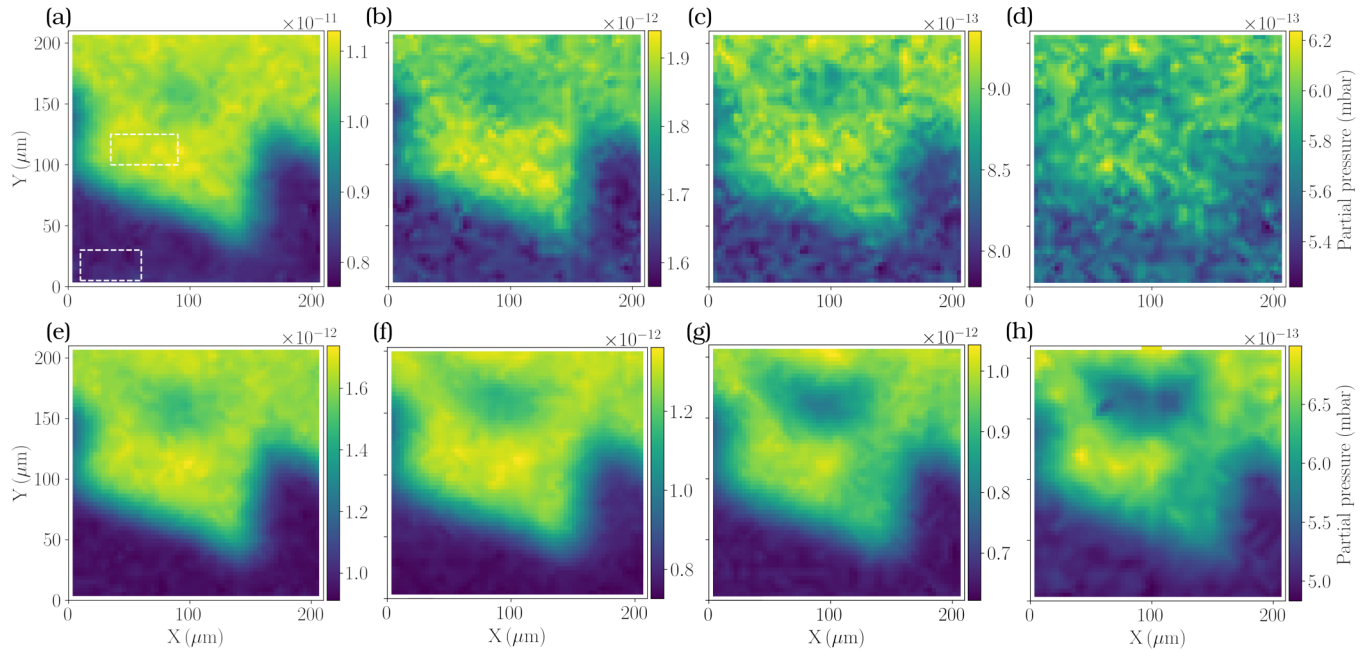
FIG. 4. (a)–(d) NAM images obtained using He at different E_{inc} for the region shown in Fig. 2(a). These measurements were performed at E_{inc} of 65, 22, 13, and 9 meV (left to right). (e)–(h) NAM images obtained using scattered Kr flux with E_{inc} of 453, 272, 194, and 124 meV (left to right). In the case of He, a steady decrease in contrast with decreasing E_{inc} is observed whereas in the case of Kr, contrast stays unchanged at higher E_{inc} [(e), (f)] and decreases at lower energies [(g), (h)].

with E_{inc} (Appendix F). For Kr, even from pristine surfaces, inelastic scattering will dominate and the scattered flux will have a broad angular distribution. At present, the width of these angular distributions and its E_{inc} dependence are unknown to us and hence an estimate of contrast, as in the case of He, cannot be made.

Another factor that needs to be considered is that of diffraction-based contrast generation. It has been reported in
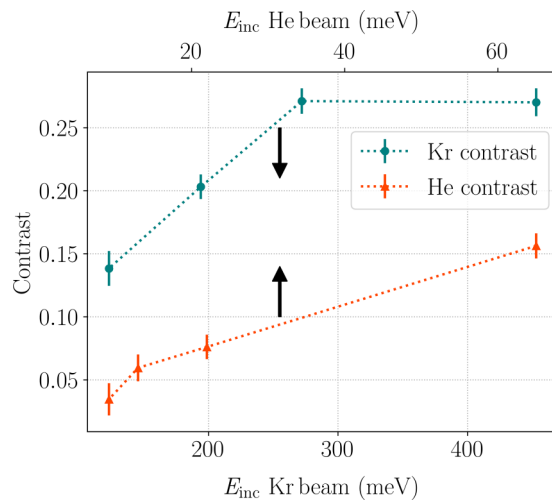

FIG. 5. Contrast obtained using He (triangles) and Kr (dots) at different E_{inc}. These values were obtained from mean signals measured in regions marked by white rectangles in Fig. 4(a), using Eq. (1). In the case of He, contrast decreases monotonically with E_{inc}. For Kr, contrast remains unchanged for 453 to 272 meV but decreases at lower energies. Error bars correspond to one standard deviation. Dashed lines are drawn as a guide to the eye for highlighting the trends.

atom-scattering-based imaging experiments that, in the case of He atom scattering from LiF(100) surfaces [18], features corresponding to diffraction can be observed from the regions where the sample is locally flat. Extending this argument, one can say that, in general, different surfaces will lead to different diffraction patterns, thereby leading to a contrast. Further, as E_{inc} decreases, diffraction peaks are expected to appear at larger angles from the specular direction. Hence, for a fixed detector geometry placed near the specular direction, this can lead to a decreasing signal (and contrast) with decreasing E_{inc}. Based on the results available for He scattering from MoS_2 surfaces [35], the first-order in-plane diffraction peaks from MoS_2 are expected to be approximately at $+/- 15°$ from the specular direction. At lower E_{inc}, these peaks are expected to move away from the specular direction and lower the signal and contrast, consistent with our observations using He. A more thorough evaluation of the role of diffraction-based contrast generation and its E_{inc} dependence can be obtained by measuring angular distributions.

A more realistic scenario for our experiments is that MoS_2 on SiO_2/Si samples have several defects and adsorbates present. Under such circumstances, a large fraction of He atoms ($> 98\%$) are expected to undergo diffuse elastic scattering. If MoS_2 surfaces have a lower defect and/or adsorbate density compared to the substrate, it will lead to a relatively lower diffuse elastic scattering component (and larger mirrorlike reflection component). This would be consistent with larger scattered signals observed from MoS_2 surfaces seen in our experiments. Further, increase in diffuse elastic scattering cross sections with decreasing E_{inc} will result in a loss of signal in the specular direction. The exact rate of this change will depend on the specific nature of surface and defects and/or adsorbates. In the case where this diffuse elastic component from the MoS_2 surface increases faster as compared to that on

SiO_2/Si, it will result in a decrease in contrast with decreasing E_{inc}, as seen in Figs. 4(a)–4(d). For Kr atoms, the already broad scattering is not expected to be influenced much with decreasing E_{inc}, leading to little or no dependence.

Different out-of-plane scattering components resulting from inelastic scattering of incident He atoms can lead to changes in specular scattered flux. Barr et al. [17] identified this effect by imaging a series of thin metal films (15 to 40 nm thickness) on SiO_2/Si surfaces using He as probe. Contrast observed in their experiments does not follow the trend expected from surface roughness (measured independently using atomic force microscopy), but decreases with decreasing incidence energy. In the present case, for He, a similar trend is observed (Figs. 4 and 5). It could well be that changes in the inelastic scattering component of He on MoS_2 and SiO_2/Si lead to an E_{inc} dependent contrast in NAM images. As mentioned earlier, Kr being relatively heavier and at larger E_{inc} than He (see Table I) is expected to undergo largely classical scattering [29,36,37]. Under these conditions, scattered flux of Kr will be relatively insensitive to surface lattice vibrations, leading to more or less unchanged contrast as observed in the 450 to 270 meV region. The decrease in contrast at lower energies could possibly arise from trapping and desorption behavior, where Kr atoms leave the surface with a very broad angular distribution, leading to a lower signal seen by our detector.

Finally, another point that needs to be looked into is that of change in surface roughness of MoS_2 versus SiO_2/Si. Although, for the current samples a direct surface roughness measurement is not available, we estimate this based on previously prepared samples using the same experimental setup and methodology. Measurements over regions with areas up to 25 μm^2 show that the surface roughness, characterized by root mean square (RMS) of the height distribution, is lower for MoS_2 (1.28 nm–1.72 nm) than SiO_2/Si (1.99 nm–3.15 nm) (see Appendix G). Assuming that a similar picture holds true for our samples, this is likely to be an important factor in contrast generation, especially when Kr atoms are used as a probe. The beam of Kr atoms being at higher E_{inc} than He is a more sensitive probe of surface roughness and the increased Kr signal from MoS_2 surface and contrast (compared to He) points toward the same. It should be noted that the contrast based purely on surface roughness is expected to be independent of E_{inc}, hence additional factors as discussed above need to be considered, especially for He atoms.

IV. CONCLUDING REMARKS

Using our recently developed NAM apparatus, we demonstrate that thin MoS_2 films up to a single monolayer on a SiO_2/Si substrate can be successfully imaged. NAM images obtained for both He and Kr exhibit a higher scattered flux from MoS_2 films compared to the underlying substrate. Observations made using Kr atoms point toward the role of decreased surface roughness caused by MoS_2 films compared to the SiO_2/Si substrate, leading to contrast generation. The decrease in contrast at lower E_{inc} possibly arises from trapping desorption of Kr atoms. On the other hand, in the case of He atoms, several factors such as changes in surface roughness,

specular component, diffuse elastic scattering, inelastic scattering, and diffraction possibly play a role. At present, based on these results alone, it is difficult to precisely evaluate the contribution of these individual factors. Nonetheless, a careful measurement of the angular distributions of the scattered flux under different conditions (E_{inc} and T_s) can provide further insights.

Our apparatus currently does not allow sample and/or detector rotation and measuring angular distributions; however, a relatively large working distance and low angular divergence of incident beam in our experiments can be utilized to set up these measurements in the future. Another interesting possibility is that of using state-of-the-art ion imaging methods [38] to measure the momentum distribution of scattered atoms. These experiments are expected to provide valuable insights into scattering dynamics and will be the focus of upcoming work in our laboratory. The nature of E_{inc}-dependent contrast obtained using Kr atoms suggests an interesting possibility of mapping different surfaces based on differential trapping probabilities. Finally, our results illustrate that the inherently sensitive nature of atom-surface scattering processes can be used in NAM for imaging films as thin as a single monolayer, opening up an important direction in its further development.

All relevant data related to the current study are available from the corresponding author upon reasonable request.

APPENDIX A: INCIDENT BEAM WIDTH MEASUREMENT

Beam width estimation corresponding to that shown in Table I of the main text. Figures 6 and 7 correspond to He and Kr beams, respectively.
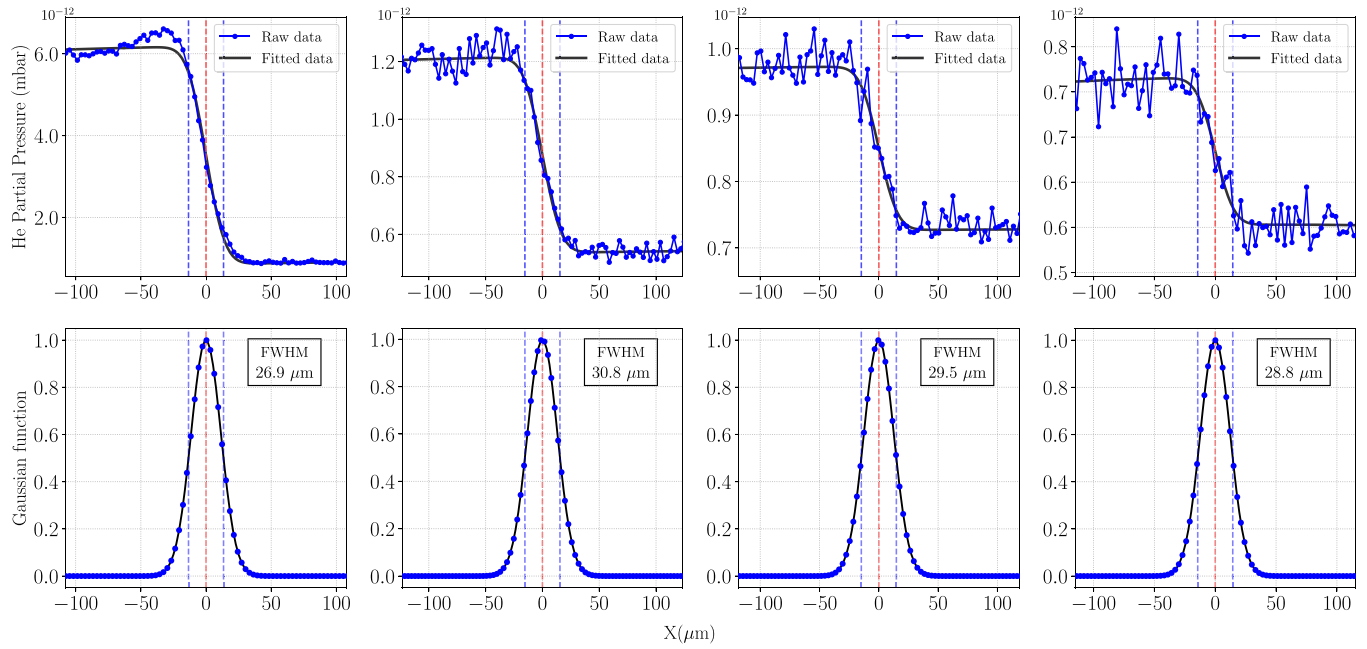
FIG. 6. Estimation of the incident beam (He) width on the sample plane using knife-edge scan method. First row (left to right), beam widths of He in the following mixtures: Pure He, 10% Kr + 90% He, 20% Kr + 80% He, 30% Kr + 70% He, respectively. Blue curve shows the He signal observed as a function of position of the knife-edge (razor blade) with step size of 3 μm. Black curve shows the best fit, using a model based on a step function convoluted with a Gaussian function with three fit parameters, namely, amplitude, center and characteristic width. The origin of x axis is shifted to center of the beam. Second row (left to right) shows the modeled beam profile with the parameters obtained by fitting.
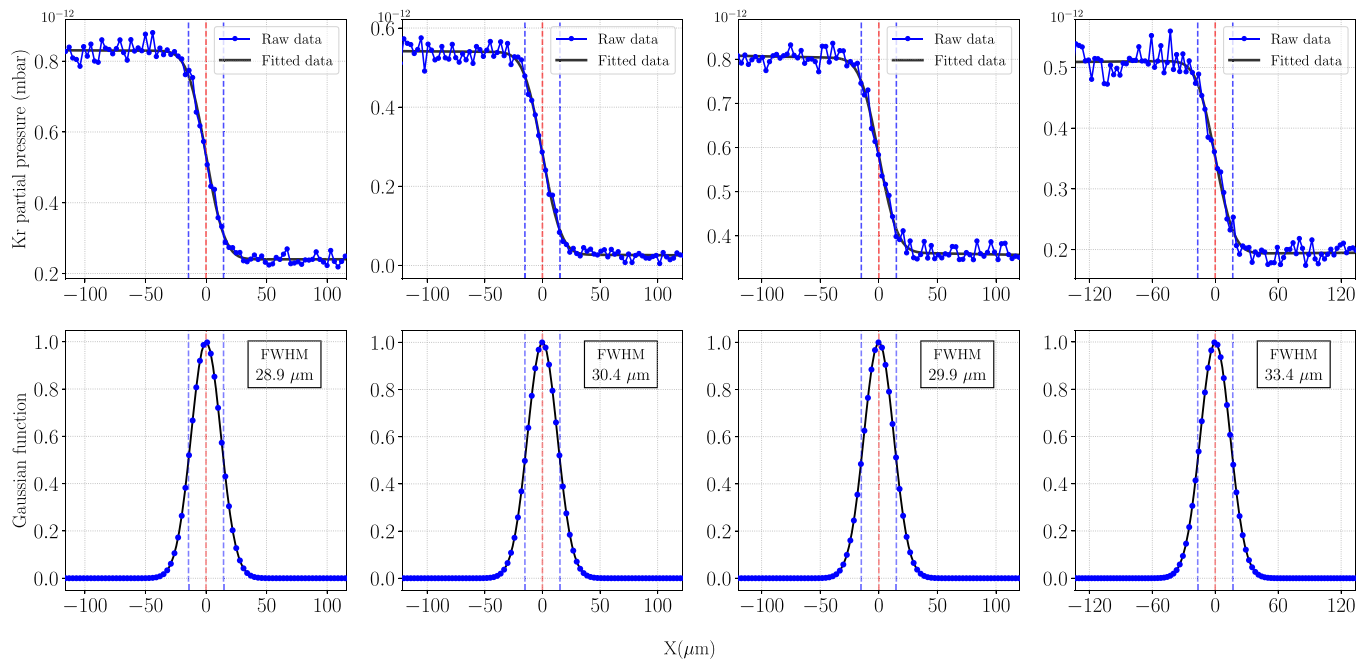

FIG. 7. Estimation of the incident beam (Kr) width on the sample plane using knife-edge scan method. First row (left to right), beam widths of Kr in the following mixtures: 10% Kr + 90% He, 20% Kr + 80% He, 30% Kr + 70% He, and 50% Kr + 50% He, respectively. Blue curve shows Kr signal observed as a function of position of the knife edge (razor blade) with step size of 3 μm. Black curve shows the best fit, using a model based on a step function convoluted with a Gaussian function, with three fit parameters, namely, amplitude, center, and characteristic width. The origin of x axis is shifted to of the beam. Second row (left to right) shows the modeled beam profile with the parameters obtained by fitting.

APPENDIX B: INCIDENT BEAM FLUX ESTIMATION

For the final collimation stage, a pinhole of 20 μm diameter has been used. Considering the change in partial pressure of gas when the beam is on and off, we estimate that 2.2×10^9 atoms/s are incident on the target surface at a backing pressure of 6 bar. The estimation is shown below:

In the transparent region (i.e., no sample in front of the final aperture):

When He beam is off; observed partial pressure
$$= 1.25 \times 10^{-12} \text{ mbar}.$$

When He beam is on; observed partial pressure
$$= 1.55 \times 10^{-12} \text{ mbar}.$$

Throughput in, Q_{in}
$$= P_{\text{steadystate}} \times \text{pumping speed}$$
$$= (1.55 \times 10^{-12} - 1.25 \times 10^{-12}) \times 300 \left(\frac{\text{mbar} \times 1}{\text{s}} \right)$$
$$= 9 \times 10^{-11} \text{mbar} \times 1 \times \frac{1}{\text{s}}.$$

The chamber volume, V, is diluted with the number of atoms, n_C, corresponding to the above pressure difference. n_c is equivalent to number of atoms incident on the surface. Simply using an ideal gas equation,

$$\Rightarrow 9 \times 10^{-11} \left(\frac{\text{mbar} \times 1}{\text{s}} \right)$$
$$= n_c \times 8.314 \times 10^{-2} \left(\frac{1 \times \text{bar}}{\text{K moles}} \right) \times 300 \text{ K}$$
$$n_c = \frac{9 \times 10^{-14}}{8.314 \times 10^{-2} \times 300} \text{ moles/s}$$
$$= 3.60 \times 10^{-15} \text{moles/s}$$
$$= 3.60 \times 10^{-15} \times 6.023 \times 10^{23} \text{ atoms/s}$$
$$= 2.2 \times 10^9 \text{ atoms/s},$$

Incident flux $= 7 \times 10^{14} \text{atoms/(s str)}.$

It should be noted that this is a lower limit estimate, given that we are measuring the pressure changes using a small, differentially pumped sampling aperture.

APPENDIX C: DETAILS OF SAMPLE PREPARATION USING CVD

A furnace-based CVD system, incorporating two temperature zones and a quartz tube where the precursors were placed, was used. N_2 was used as the carrier gas with a flow rate of 200 SCCM during the entire process (Fig. 8). This also provides a chemically inert environment. A low temperature zone, containing sulfur powder, was maintained at 200 °C.
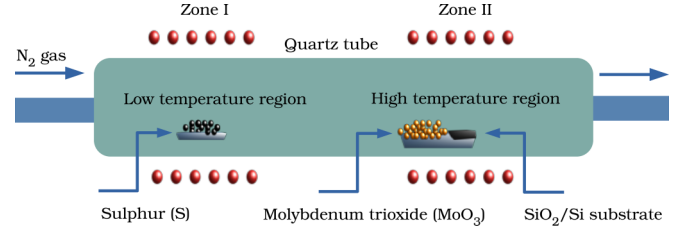

FIG. 8. A schematic of the setup used for chemical vapor deposition (CVD) having two temperature zones. Precursors are placed at a distance of around 10 cm from each other. Carrier gas, i.e., N_2, is allowed to flow from low to high temperature region for the growth of atomically thin layers of MoS_2.

MoO_3, placed in an alumina crucible, was kept in the high temperature zone beside a SiO_2/Si substrate at 650 °C. It took around 30 min for the high-temperature zone to reach 650 °C. The actual growth process took around 15 minutes. To arrest the growth, the furnace was opened straight away to cool it down to room temperature (Fig. 9).

APPENDIX D: SAMPLE CHARACTERIZATION WITH RESPECT TO TIME

Contrast obtained for MoS_2 versus SiO_2/Si using He (pure He beam, $E_{inc} = 65$ meV) measured over a span of six days is shown in Figs. 10(a)–10(c). Contrast observed for thin MoS_2 films, corresponding to regions A_1, A_2 and B_1, B_2 remain largely unchanged over this time span [Fig. 10(d)]. On the other hand, the contrast measured at different E_{inc} (from regions A_1, A_2) during the same time span shows a much larger change, clearly decreasing with E_{inc}. These measurements correspond to the same region of sample as shown in Fig. 4 of the main text.
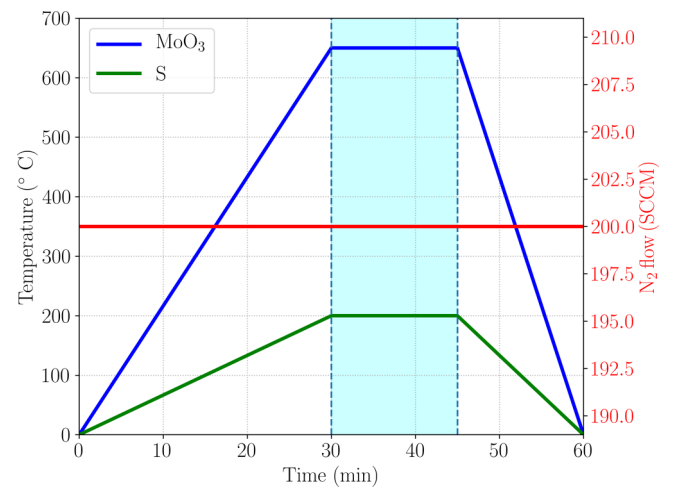

FIG. 9. A profile of temperature with time for CVD growth of MoS_2. MoO_3 placed in high temperature zone takes around 30 min to reach 650° and sulfur powder placed in low temperature zone reaches 250° in the same time. The growth process takes approximately 15 min. These are optimized temperatures based on the vapor pressure of precursors.
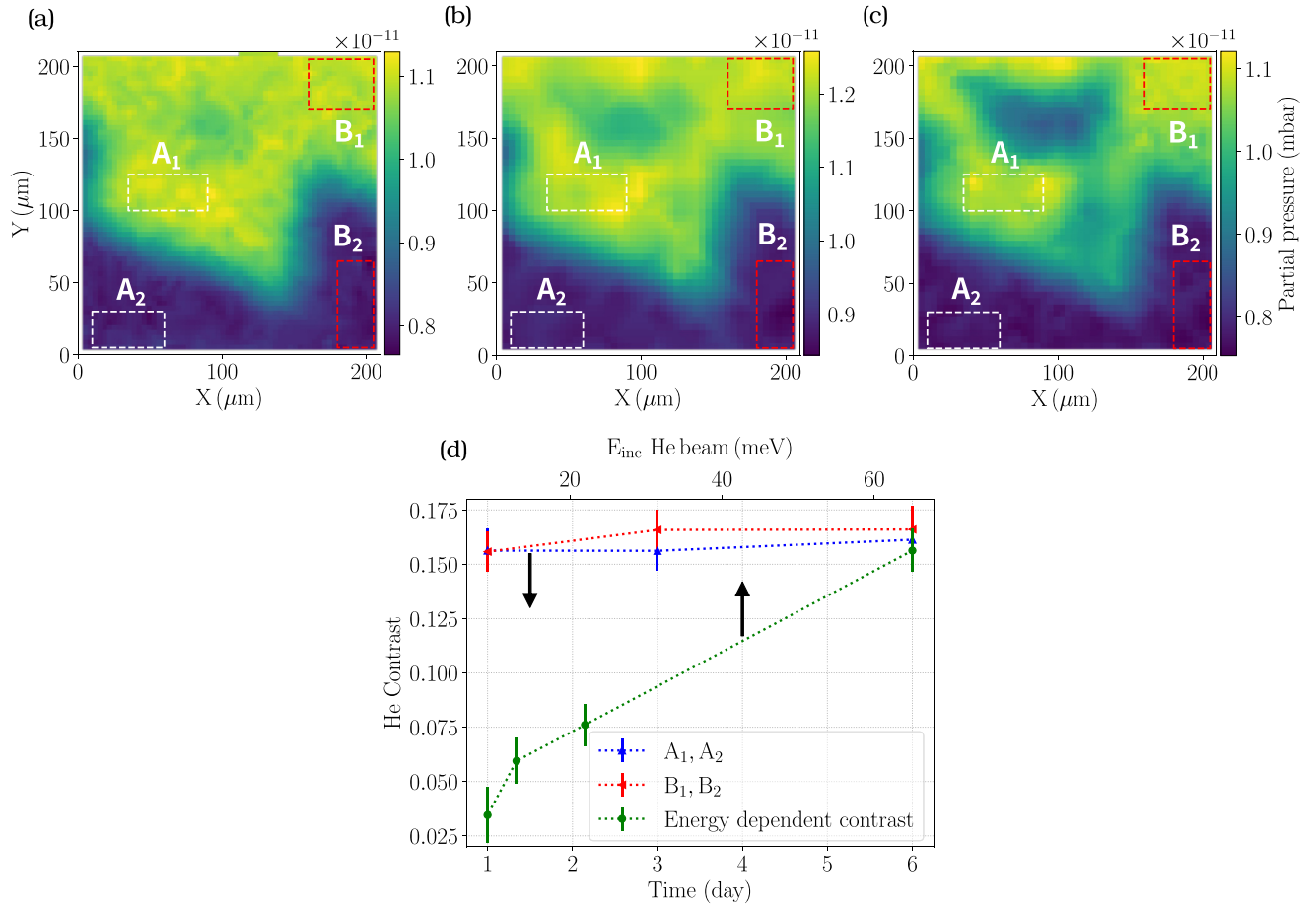
FIG. 10. NAM images and contrast measured using He over a time span of several days. (a)–(c) NAM images (pure He beam at $E_{inc} =$ 65 meV) measured at day 1, 3, and 6 after the sample placed in the vacuum chamber. (d) Blue and red points show the contrast evaluated from the above images. For comparison, contrast versus E_{inc} measured during the same time span is also shown (green points). Contrast is calculated using the signals obtained from regions marked by rectangles and labeled as A_1, A_2 and B_1, B_2 in (a)–(c) Here A_1, B_1 and A_2, B_2 correspond to thin MoS$_2$ films and substrate, respectively. Dashed lines are drawn as a guide to the eye for highlighting the trends.

APPENDIX E: LIST OF PEAK POSITIONS IN RAMAN SPECTRA

The following table shows the peak positions observed in the Raman spectra corresponding to E_{2g}^1 and A_{1g} modes in

MoS$_2$ and that for substrate SiO$_2$. Figure numbers in this table correspond to that in the main text.

|	E_{2g}^1 (cm^{-1})	A_{1g} (cm^{-1})	$(E_{2g}^1 - A_{1g})$ cm^{-1}	SiO$_2$ peak (cm^{-1})
Figure 2				
MoS$_2$ thin layer	385.80	405.31	19.51	520.86
MoS$_2$ thick layer	383.97	409.48	25.51	520.69
Bare substrate				520.86
Figure 3(a)				
MoS$_2$ thin layer	385.97	405.15	19.17	520.86
MoS$_2$ thick layer	383.80	408.81	25.01	520.86
Bare substrate				520.86
Figure 3(b)				
MoS$_2$ thin layer	383.82	404.46	20.64	520.47
MoS$_2$ thick layer	382.49	408.73	26.24	520.74
Bare substrate				520.47
Figure 3(c)				
MoS$_2$ thin layer	384.97	404.98	20.01	520.86
MoS$_2$ thick layer	383.47	409.65	26.18	520.86
Bare substrate				520.86
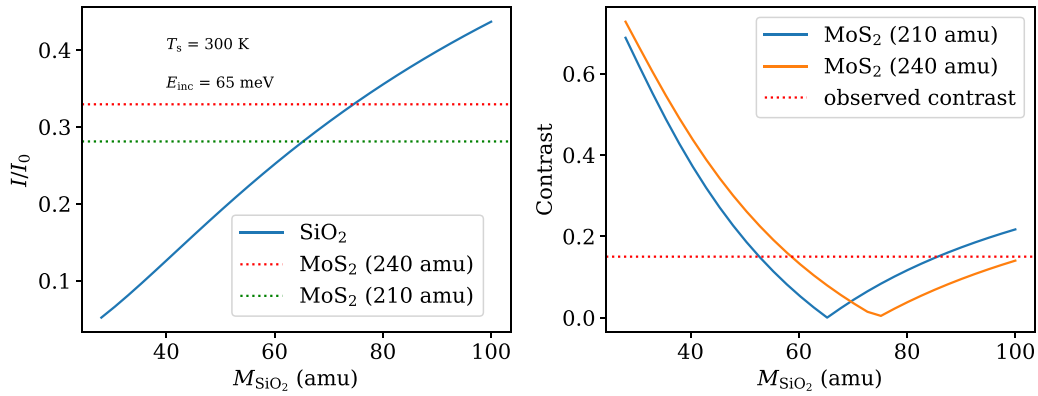
FIG. 11. Left: A plot of the specular intensity (I/I_0) calculated using Debye waller factor with different surface masses for SiO$_2$. The horizontal dashed lines show the specular intensity calculated for MoS$_2$ using surface masses 210 and 240 amu. Right: Dependence of the calculated contrast on the surface mass of SiO$_2$. Surface temperature of 300 K and E_{inc} of 65 meV is used for these calculations. Based on the experimental observations, where the specular reflected signal from MoS$_2$ is higher than substrate by approximately 30% and the contrast about 15%, we estimate that effective surface mass of approximately 60 amu seems appropriate.
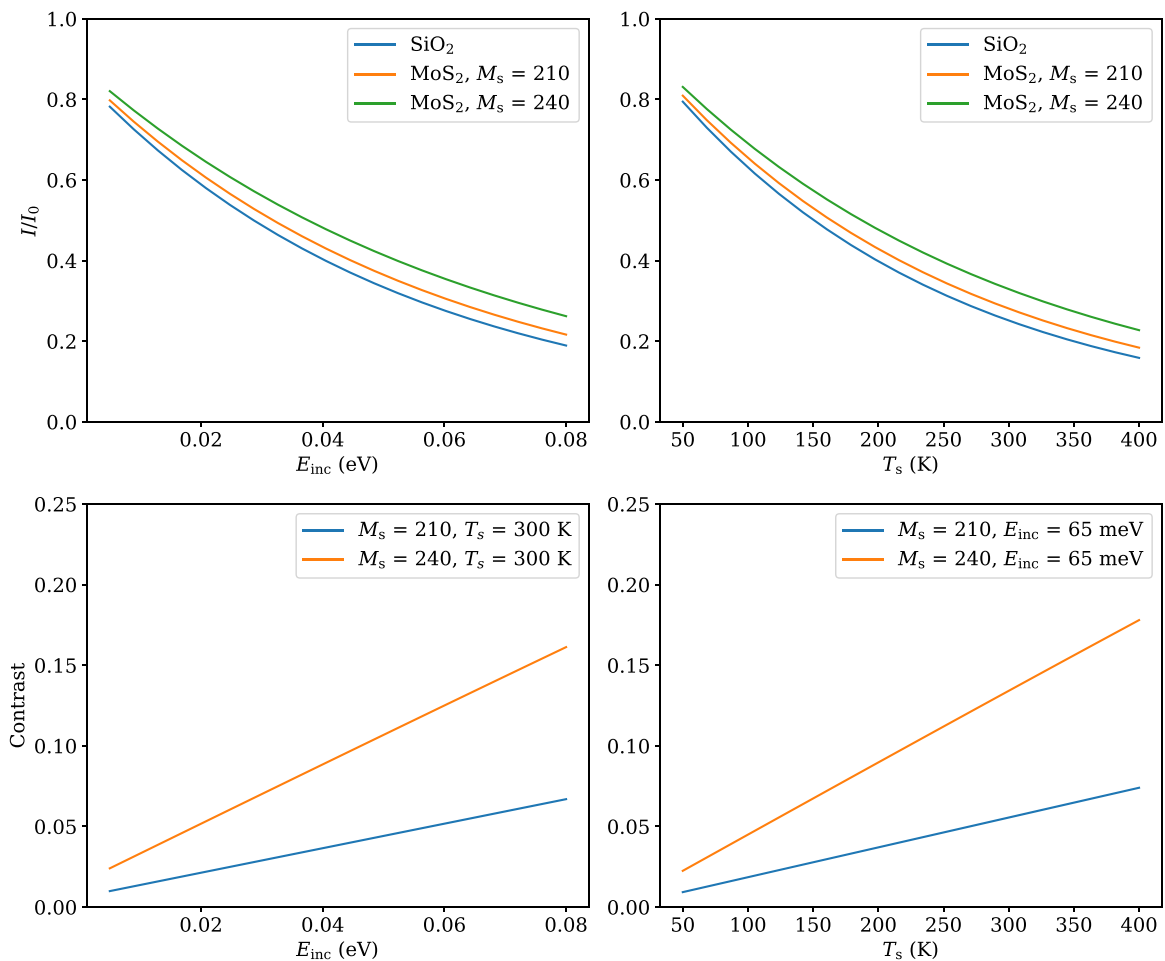

FIG. 12. The specular intensities and contrasts are calculated as a function of surface temperature and incidence energy. A surface mass of 60 amu for SiO$_2$ is used (based on the estimation in Fig. 11). Top row: The specular intensity estimated for MoS$_2$ (using two different surface masses) and SiO$_2$. Specular intensity decreases with increasing incidence energy and surface temperature. Bottom row: Estimated contrast increases with increasing incidence energy (at surface temperature = 300 K) and also with surface temperature (at incidence energy = 65 meV).
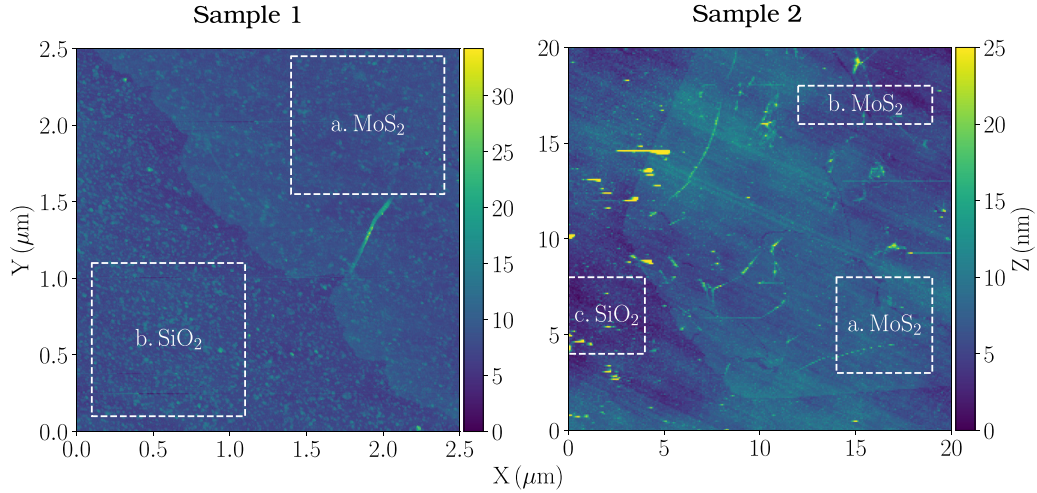
FIG. 13. AFM images of two different samples prepared (prepared independently) using the same method and experimental setup (note the different sample sizes). On sample 1, we selected a region of $\sim (1 \times 1)\,\mu$m on MoS$_2$ and SiO$_2$ as well. Relatively large areas $\sim (5 \times 5)\,\mu$m were selected on sample 2 to calculate the RMS roughness. These regions are indicated by white dashed rectangles.

APPENDIX F: ESTIMATION OF SPECULAR REFLECTED INTENSITIES CONSIDERING PRISTINE SURFACES

Contrast estimation assuming pristine surfaces, where the changes in specular intensity alone is the major factor, can be estimated using Debye Waller factors [using Eqs. (3) and (4) in the main text]. This requires the masses of surface atoms to be known. In the present case of MoS$_2$ and SiO$_2$/Si (unlike elemental surfaces comprising a single type of atom) we estimate the effective surface mass in the following manner:
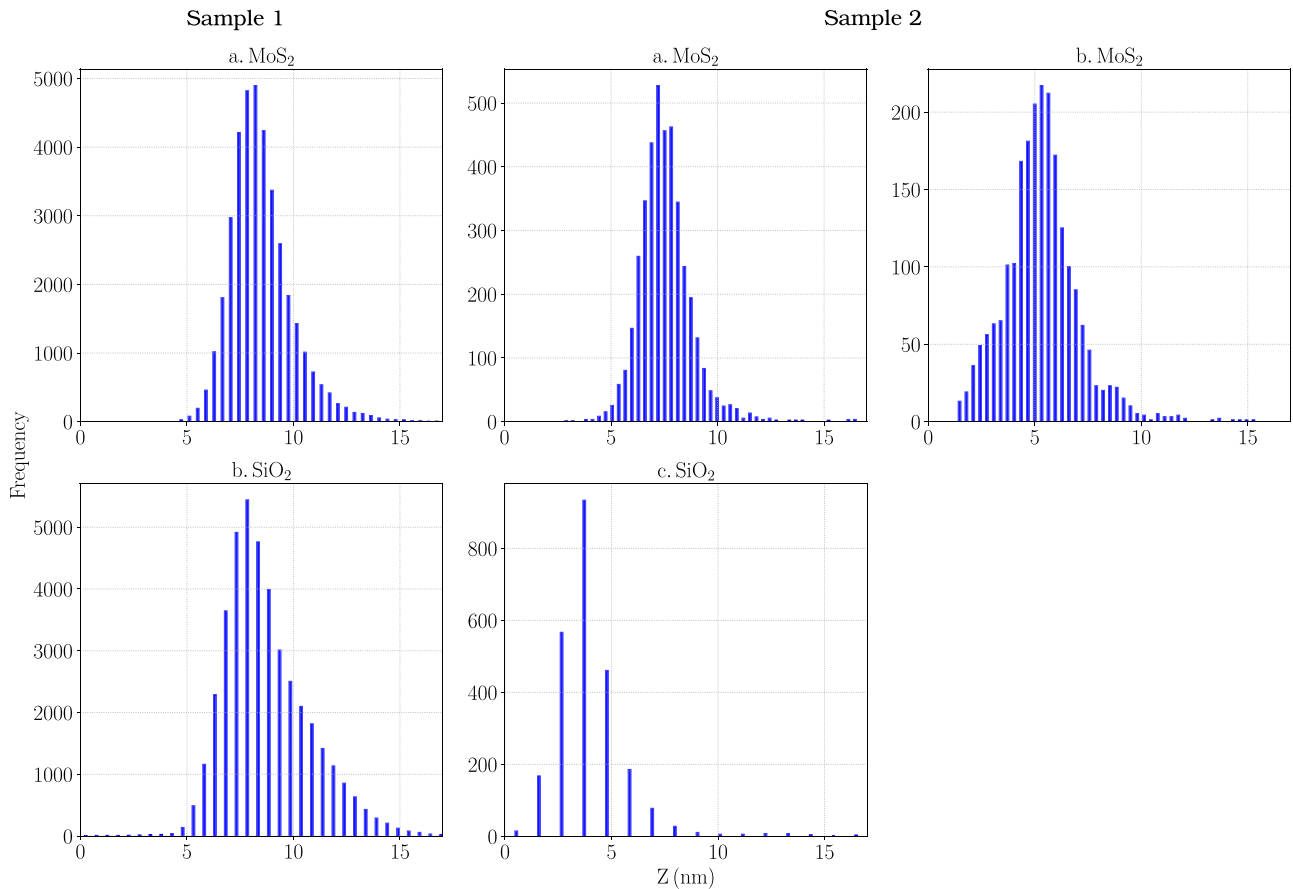

FIG. 14. The corresponding histograms of the marked regions in Fig. 13 (above). The *X* and *Y* axis in all graphs correspond to the height (*Z*) in nm and the frequency, respectively.

The available data of specular scattering versus T_s has been reported in Ref. [36]. A fit to this data (two curves) using the surface mass as fit parameter gives the effective mass of MoS_2 surface to be 210 and 240 amu. For SiO_2, such data is not available to the best of our knowledge. However, a reasonable guess can be made based on the constraints available from our results.

Our experiments show that the scattered signal from MoS_2 surfaces is higher than SiO_2/Si by approximately 30%, and the typical contrast being 15%, we can narrow down the range of effective mass of the SiO_2 surface. Estimations depicted in Fig. 11 show that given the above constraints, the surface mass for SiO_2/Si will be in the range of 50–60 amu.

For the parameters chosen and within the validity of the framework where contrasts depend solely on specular scattered signals, contrast is expected to increase at higher E_{inc} and also with increasing surface temperature (Fig. 12, bottom row).

APPENDIX G: ATOMIC FORCE MICROSCOPY (AFM) BASED ROUGHNESS ESTIMATION

The following table shows RMS roughness calculated corresponding to MoS_2 and SiO_2 regions in two different samples (Figs. 13 and 14). It shows that the surface roughness for MoS_2 is lower than the substrate. These measurements were carried out using the AFM (Dimension Icon, Bruker) at Weizmann Institute of Science, Israel.

	Regions	RMS roughness (nm)
Sample 1	a. MoS_2	1.45
	b. SiO_2	1.99
Sample 2	a. MoS_2	1.28
	b. MoS_2	1.72
	c. SiO_2	3.15

[1] D. B. Murphy, *Fundamentals of Light Microscopy and Electronic Imaging* (John Wiley & Sons, New York, 2002).

[2] E. Ruska, The development of the electron microscope and of electron microscopy, Biosci. Rep. **7**, 607 (1987).

[3] W. Gao, C. Addiego, H. Wang, X. Yan, Y. Hou, D. Ji, C. Heikes, Y. Zhang, L. Li, H. Huyan *et al.*, Real-space charge-density imaging with sub-Å resolution by four-dimensional electron microscopy, Nature (London) **575**, 480 (2019).

[4] D. Rugar and P. Hansma, Atomic force microscopy, Phys. Today **43**(10), 23 (1990).

[5] P. Eaton and P. West, *Atomic Force Microscopy* (Oxford University Press, 2010).

[6] G. Binnig, H. Rohrer, C. Gerber, and E. Weibel, Surface Studies by Scanning Tunneling Microscopy, Phys. Rev. Lett. **49**, 57 (1982).

[7] G. Binnig and H. Rohrer, Scanning tunneling microscopy, Surf. Sci. **126**, 236 (1983).

[8] D. A. MacLaren, B. Holst, D. J. Riley, and W. Allison, Focusing elements and design considerations for a scanning Helium microscope (SHeM), Surf. Rev. Lett. **10**, 249 (2003).

[9] P. Witham and E. Sánchez, A simple approach to neutral atom microscopy, Rev. Sci. Instrum. **82**, 103705 (2011).

[10] A. Fahy, M. Barr, J. Martens, and P. C. Dastoor, A highly contrasting scanning Helium microscope, Rev. Sci. Instrum. **86**, 023704 (2015).

[11] P. Witham and E. Snchez, Exploring neutral atom microscopy: Exploring neutral atom microscopy, Cryst. Res. Technol. **49**, 690 (2014).

[12] I. Estermann and O. Stern, Beugung von molekularstrahlen (Diffraction of molecular beams), Z. Phys. **61**, 95 (1930).

[13] M. Bergin, D. J. Ward, S. M. Lambrick, N. A. von Jeinsen, B. Holst, J. Ellis, A. P. Jardine, and W. Allison, Low-energy electron ionization mass spectrometer for efficient detection of low mass species, Rev. Sci. Instrum. **92**, 073305 (2021).

[14] A. S. Palau, G. Bracco, and B. Holst, Theoretical model of the Helium pinhole microscope, Phys. Rev. A **94**, 063624 (2016).

[15] A. S. Palau, G. Bracco, and B. Holst, Theoretical model of the Helium zone plate microscope, Phys. Rev. A **95**, 013611 (2017).

[16] B. Holst and W. Allison, An atom-focusing mirror, Nature (London) **390**, 244 (1997).

[17] M. Barr, A. Fahy, J. Martens, A. P. Jardine, D. J. Ward, J. Ellis, W. Allison, and P. C. Dastoor, Unlocking new contrast in a scanning Helium microscope, Nat. Commun. **7**, 10189 (2016).

[18] M. Bergin, S. M. Lambrick, H. Sleath, D. J. Ward, J. Ellis, and A. P. Jardine, Observation of diffraction contrast in scanning Helium microscopy, Sci. Rep. **10**, 2053 (2020).

[19] D. Farías and K. H. Rieder, Atomic beam diffraction from solid surfaces, Rep. Prog. Phys. **61**, 1575 (1998).

[20] P. Sutter, M. Minniti, P. Albrecht, D. Farías, R. Miranda, and E. Sutter, A high-reflectivity, ambient-stable graphene mirror for neutral atomic and molecular beams, Appl. Phys. Lett. **99**, 211907 (2011).

[21] G. Scoles, *Atomic and Molecular Beam Methods* (Oxford University Press, New York, 1988).

[22] H. O. Pierson, *Handbook of Chemical Vapor Deposition: Principles, Technology and Spplications* (William Andrew, Norwich, New York, 1999).

[23] D. M. Popovic, V. Milosavljevic, A. Zekic, N. Romcevic, and S. Daniels, Raman scattering analysis of silicon dioxide single crystal treated by direct current plasma discharge, Appl. Phys. Lett. **98**, 051503 (2011).

[24] J. L. Verble and T. J. Wieting, Lattice Mode Degeneracy in MoS_2 and Other Layer Compounds, Phys. Rev. Lett. **25**, 362 (1970).

[25] C. Lee, H. Yan, L. E. Brus, T. F. Heinz, J. Hone, and S. Ryu, Anomalous lattice vibrations of single-and few-layer MoS_2, ACS Nano **4**, 2695 (2010).

[26] H. Li, Q. Zhang, C. C. R. Yap, B. K. Tay, T. H. T. Edwin, A. Olivier, and D. Baillargeat, From bulk to monolayer MoS_2: evolution of Raman scattering, Adv. Funct. Mater. **22**, 1385 (2012).

[27] B. Holst and G. Bracco, Probing surfaces with thermal He atoms: Scattering and microscopy with a soft touch, in *Surface Science Techniques* (Springer, 2013), pp. 333–365.

[28] G. Comsa, The applicability of the Debye-Waller factor to the He scattering from metal surfaces, J. Phys. C: Solid State Phys. **6**, 2648 (1973).

[29] E. K. Schweizer and C. T. Rettner, Quantum Effects in the Scattering of Argon from 2H-W(100), Phys. Rev. Lett. **62**, 3085 (1989).

[30] G. Anemone, A. Al Taleb, S. D. Eder, B. Holst, and D. Farías, Flexible thin metal crystals as focusing mirrors for neutral atomic beams, Phys. Rev. B **95**, 205428 (2017).

[31] E. K. Schweizer, C. T. Rettner, and S. Holloway, Diffraction and rainbows in the scattering of argon from 2H-W(100), Surf. Sci. **249**, 335 (1991).

[32] C. T. Rettner, J. A. Barker, and D. S. Bethune, Angular and Velocity Distributions Characteristic of the Transition Between the Thermal and Structure Regimes of Gas-Surface Scattering, Phys. Rev. Lett. **67**, 2183 (1991).

[33] D. Kulginov, M. Persson, C. T. Rettner, and D. S. Bethune, An empirical interaction potential for the Ar/Pt(111) system, J. Phys. Chem. **100**, 7919 (1996).

[34] B. Poelsema, R. L. Palmer, S. T. De Zwart, and G. Comsa, Thermal energy helium scattering from CO/Pt (111) at very low coverages, Surf. Sci. **126**, 641 (1983).

[35] G. Anemone, A. Al Taleb, G. Benedek, A. Castellanos-Gomez, and D. Farías, Electron-âphonon coupling constant of 2H-MoS_2(0001) from helium-atom scattering, J. Phys. Chem. C **123**, 3682 (2019).

[36] T. Andersson, F. Althoff, P. Linde, S. Andersson, and K. Burke, Probing a cold surface with slow heavy-atom scattering: Experimental results and theoretical calculations, Phys. Rev. B **65**, 045409 (2002).

[37] J. M. Moix and E. Pollak, Communication: Heavy atom quantum diffraction by scattering from surfaces, J. Chem. Phys. **134**, 011103 (2011).

[38] D. J. Harding, J. Neugebohren, D. J. Auerbach, T. N. Kitsopoulos, and A. M. Wodtke, Using ion imaging to measure velocity distributions in surface scattering experiments, J. Phys. Chem. A **119**, 12255 (2015).